Nuclear Science and Techniques (2025) 36:99
https://doi.org/10.1007/s41365-025-01676-6

Temperature effects on strain distribution of reduced-activation ferritic/martensitic steel during tensile tests

Shang-Ming Chen[1,2] · Cheng-Jun Zhu[1,2] · Yi-Fan Shi[1,2] · Lei Peng[1,2] · Jing-Yi Shi[1,2] · Yong-Jie Sun[1,2] · Ye-Shang Hu[1,2] · Yi-Fei Liu[1,2] · Zhen-Yu Wei[1,2]

Received: 11 April 2024 / Revised: 28 May 2024 / Accepted: 13 June 2024 / Published online: 19 April 2025

Abstract
The reduced-activation ferritic/martensitic (RAFM) steel CLF-1 has been designed as a candidate structural material for nuclear fusion energy reactors. For engineering mechanical design, the effects of temperature on the strain distribution of CLF-1 steel during uniaxial tensile tests were explored within the temperature range from room temperature to 650 °C using uniaxial tensile tests combined with in situ digital image correlation analysis. Strain-concentrated regions alternately distributed ± 45° along the tensile direction could be attributed to the shear stress having the maximum value at ± 45° along the tensile direction and the coordinated deformation of the microstructure. The total strain distribution changed from a normal distribution to a lognormal distribution with increasing deformation owing to the competition between the elastic and plastic strains at all test temperatures. Strain localization has a strong relationship with temperature at the same engineering strain because of the temperature effects on dynamic strain aging (DSA). The stronger the DSA effect, the stronger the strain localization. With increasing temperature, the stronger the strain localization at the same strain, the weaker the plasticity, that is, DSA-induced embrittlement, and the slower the strength decline, that is, DSA-induced hardening.

Keywords RAFM steel · Tensile test · Strain distribution · Temperature effect

1 Introduction

Currently, more than 80% of energy [1] is produced from non-renewable resources, such as gas, coal, and oil. Energy shortages and environmental pollution are two major problems in social development. Increasing attention has been given to nuclear fusion energy because of its advantages such as cleanliness and abundant raw materials. Nuclear fusion power reactors can potentially produce large amounts of clean energy [2], which can solve the energy shortage problem faced by humans. However, harnessing fusion energy is difficult [3]. The behavior of materials inside the reactor determines the success or failure of nuclear technology [4]. Reduced-activation ferritic/martensitic (RAFM) steels are promising structural materials for fusion power reactor blanket modules because of their high creep resistance, high fatigue resistance, good weldability, high strength, high toughness, low activation, high swelling resistance, and high neutron irradiation embrittlement resistance [5–9]. Considering the design and function of test blanket modules (TBMs) of a clear fusion energy reactor, structural steels will function at 300–550 °C for a long time [10–12]. Therefore, when a nuclear fusion energy reactor begins operation, the structural steels will operate at a range of temperatures (25–650 °C). The anisotropy of polycrystalline materials can create inhomogeneities at the grain scale (mesoscale), even under the same deformation conditions [13]. Thus, exploring the deformation behavior at different

Chen and Zhu the authors contributed equally to this work.

This work was supported by the National Natural Science Foundation of China (Nos. 12175231 and 11805131), Anhui Natural Science Foundation of China (No. 2108085J05), and the Collaborative Innovation Program of Hefei Science Center, CAS (No. 2022HSC-CIP009).

✉ Lei Peng
penglei@ustc.edu.cn

[1] School of Nuclear Science and Technology, University of Science and Technology of China, Hefei 230027, China

[2] State Key Laboratory of Particle Detection and Electronics, University of Science and Technology of China, Hefei 230026, China

temperatures of RAFM steels at the grain scale (mesoscale) is very important for engineering mechanical design.

The crystal plasticity finite element method (CPFEM) can reflect the microstructure of polycrystalline materials by combining the finite element and crystal plasticity theories [14, 15]. It can consider various deformation mechanisms at the grain scale (mesoscale), such as deformation twinning, dislocation slip, and phase transition [16–18]. Moreover, it can explore the plastic deformation mechanisms of polycrystalline materials at the microstructural level . Recently, the relationships between the non-uniform evolution of microstructures and macroscopic homogenization mechanical properties have been widely explored using the CPFEM [19–23]. Tasan et al. [24] explored strain localization and damage by combining the CPFEM and deformation experiments on dual-phase steel. Zhao et al. [22] investigated the evolution of face-centered-cubic polycrystalline plastic anisotropy during biaxial loading using the CPFEM. Abdolvand et al. [21] developed a crystal plasticity finite element code to explore the deformation behavior of hexagonal close packed materials. Modeling is a very important task when using the CPFEM for simulation. To the best of our knowledge, every material has a critical window, that is, a minimum statistical representative window (MSRW) that can be used as the lowest limit of a representative volume element (RVE) [25, 26]. At the MSRW, a material exhibits macroscopic homogeneity during deformation experiments. Thus, the "average" properties of a material can be studied only if a sufficiently large model is built. Thus, the relationship between the microstructure (at the mesoscale) and mechanical properties (at the macroscale) can be explored. However, determining the MSRW is a difficult task [27–29]. Koohbor et al. [28] used an experimental method to determine the RVE size in woven composites, observing that if the average local strain of the selected window is the same as the global strain, the size of the selected window is identified as the MSRW, that is, the RVE size. Using numerical experiments and statistical analyses, Mirkhalaf et al. [29] developed a method for determining the RVE size in heterogeneous amorphous materials. Although methods for determining the RVE size have been proposed in the abovementioned studies, they are difficult to use in practice. Fortunately, Tang et al. [30] proposed a universal law for plastic deformation, that is, the lognormal strain distribution during plastic deformation. Macroscopic homogeneity during deformation experiments in the sample window of interest can be quantitatively measured using lognormal distribution statistics. The larger the coefficients of determination, the better the macroscopic homogeneity during deformation. Thus, the strain distribution in the deformation process of a material should be studied to establish the finite element model using the CPFEM. The macroscopic homogeneity on the sample window scale has been discussed by Zhi et al. [31], Chen et al. [32], Dhekne et al. [33], and Peng et al. [34] using strain distribution during deformation. Although the strain distribution during deformation has been studied both through experiments and simulations, the temperature has been limited to room temperature (R.T.), and the effect of temperature on the strain distribution during deformation has not been studied so far. Moreover, no study has been conducted on the strain distribution of RAFM steel, either through experiments or simulations. Thus, the effect of temperature on the strain distribution of RAFM steel during deformation should be explored to establish a finite element model using the CPFEM in future research.

In this study, uniaxial tensile tests combined with digital image correlation (DIC) were used to explore the effect of the test temperature on the strain (e_{yy}) distribution of CLF-1 steel during deformation. The evolution of the strain statistics and strain localization with increasing temperature was analyzed in detail. These results provide a significant reference for the mechanical engineering design of fusion energy reactors.

2 Material and method

2.1 Material

The CLF-1 steel used in this study was produced using a vacuum induction method. The studied steel was manufactured from a 5-t ingot. The measured chemical composition of the steel was 8.49 Cr-1.50 W-0.22 V-0.09 Ta-0.50 Mn-0.13 C-Fe in wt%. Finally, the steel was supplied as plates that were hot-rolled to a thickness of 30 mm. The as-received (AR) steel was heat-treated via normalization and tempering (NT). The normalization process was performed at 980 ℃ for 3.6 ks, and the cooling method was water cooling; subsequently, the tempering process was performed at 740 ℃ for 7.2 ks, and the cooling method was air cooling. The microstructure revealed equiaxed grains, and the prior austenite grain size was approximately 14 μm (Fig. 1a, b). The studied steel had an all martensitic structure, as depicted in Fig. 1a–c. The elemental distributions are presented in Fig. 1d.

2.2 Uniaxial tensile test

Typically, tensile tests of irradiated specimens use small tensile specimens. For further comparison with the tensile test data of irradiated specimens, miniature flat tensile specimens, which were consistent with "small tensile materials" in the SINQ Target Irradiation Program (STIP) [35–39], were fabricated from plate as shown in Fig. 2. The specimens had a geometry of 5.0 mm gauge length, 0.40 mm

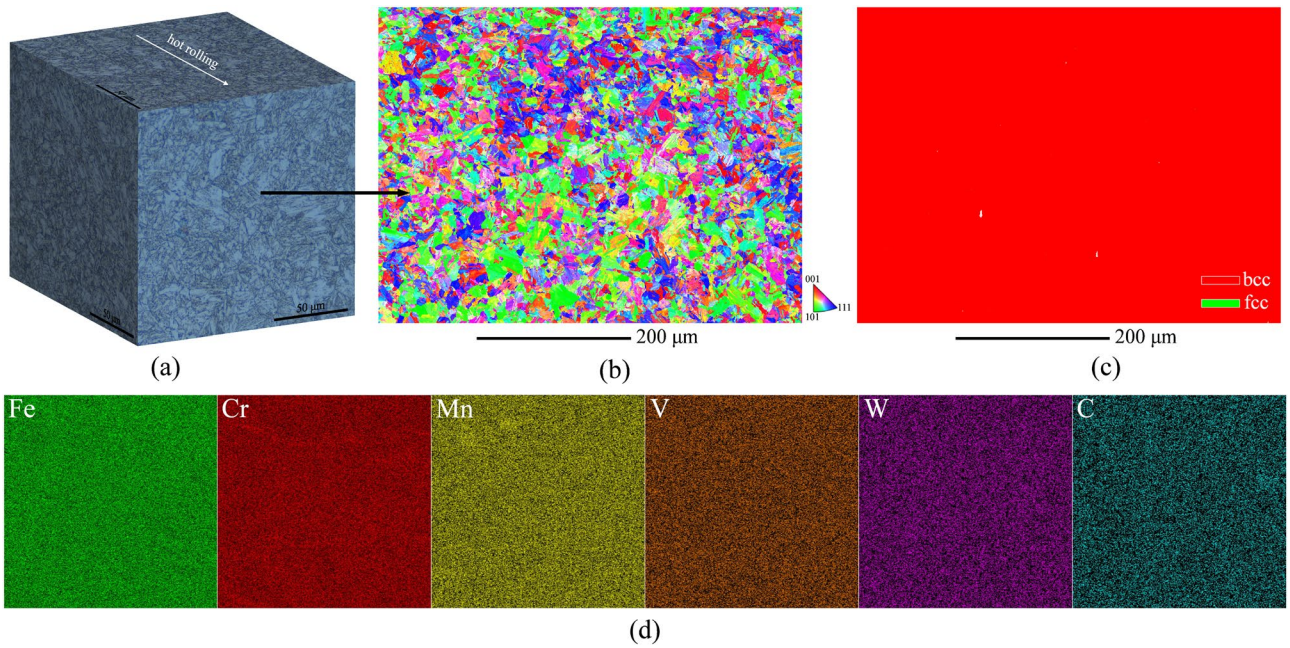

Fig. 1 (Color online) **a** Photomicrograph, **b** SEM/EBSD images, **c** phase mapping, and **d** corresponding EDX mapping of CLF-1 steel

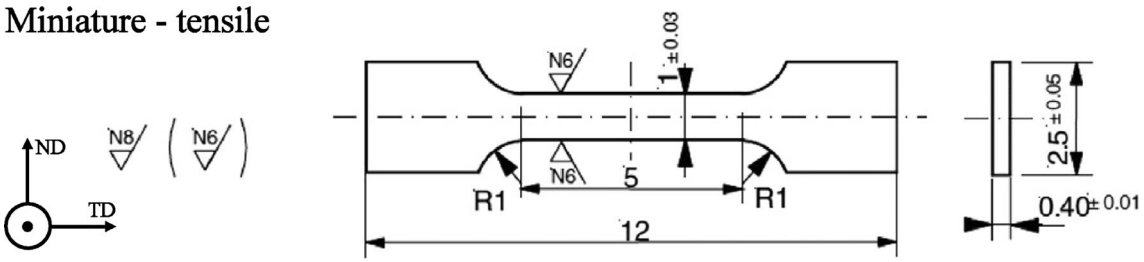

Fig. 2 Dimensions of miniature flat tensile specimens of RAFM steel CLF-1. (in mm)

thickness, and 1.00 mm width. Before the tensile tests, the dimensions of each specimen were measured precisely.

Uniaxial tensile tests were performed on an MTS mechanical testing machine with a capacity of 10-kN force, which was equipped with a video extensometer. The experiments were conducted in a vacuum, the strain rate was set to 1×10^{-3} s^{-1}, and the test temperature range was 25–650 ℃. Before the tensile test, the specimens were maintained at a set temperature for 3.6 ks. The accuracy of the force measurements was within ±0.1%. DIC [40, 41] was used to measure the full-field displacement (or full-field strain). The DIC system, as depicted in Fig. 3a, b, consisted of one LED light and one FLIR camera with a resolution of 0.006 mm/pixel equipped with a lens (Schneider-KREUZNACH). The speckles shown in Fig. 3c were formed using spray painting [42]. The image acquisition rate was 1 Hz. A schematic of the full-field strain in the form of a contour plot during tensile testing is shown in Fig. 3d. The strain (e_{yy}) discussed in this paper was along the tensile direction. Experiments were performed twice at each temperature to ensure reproducibility.

2.3 Strain error evaluation

The specimen surface under zero-strain conditions was photographed twice to evaluate the errors. Ideally, displacement should be null under zero-strain conditions. However, inevitable micro-movements of the experimental components would result in micro-displacement during an actual experiment. The micro-strain generated by this micro-displacement is considered an error. This error consists of systematic and random errors. "Accuracy" reflects systematic errors, whereas "precision" reflects random errors [43]. The mean absolute error (MAER) and standard deviation of error (SDER) are computed using Eqs. (1) and (2) [44] to represent systematic and random errors, respectively.

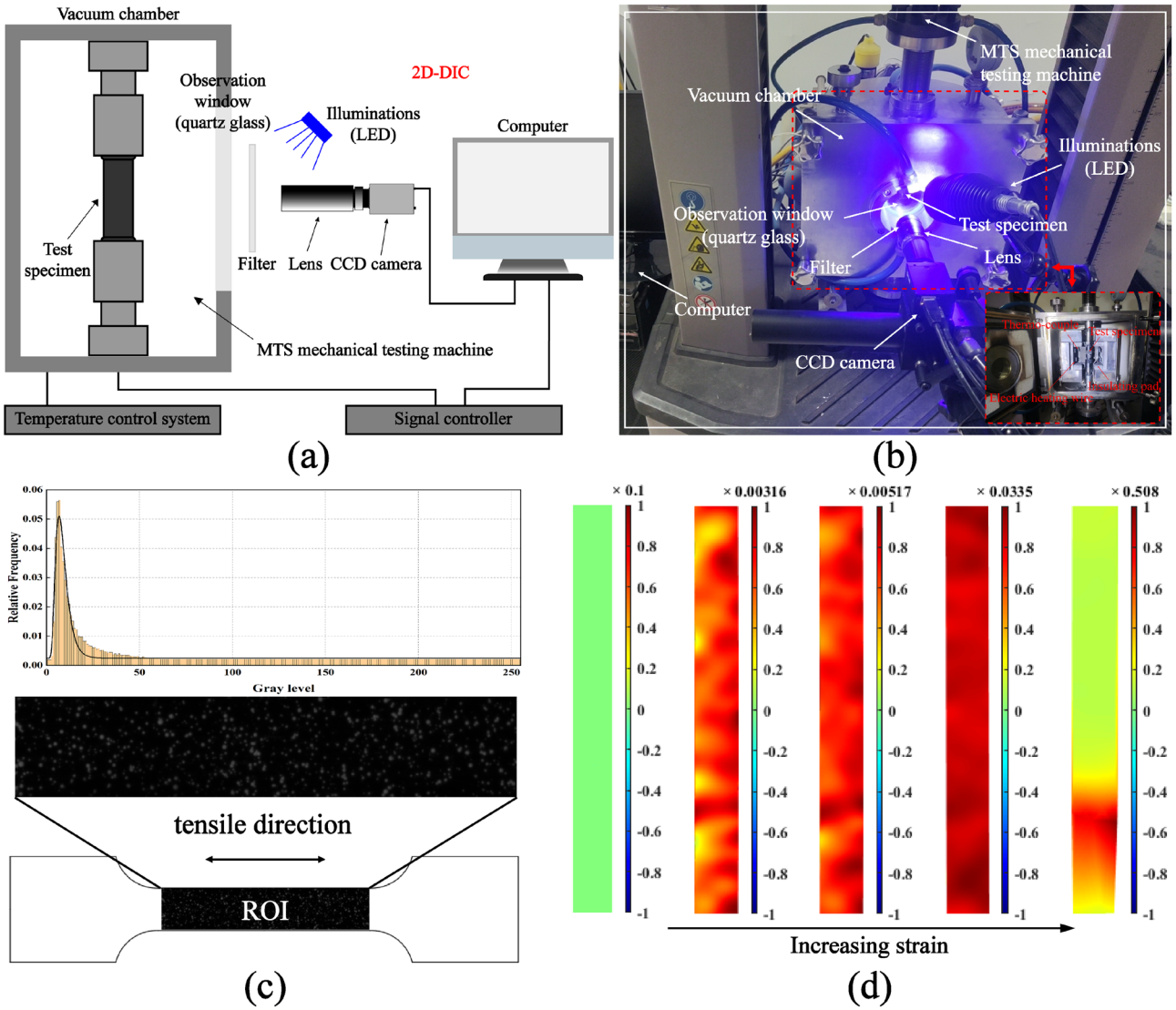

Fig. 3 (Color online) **a** Diagram of the DIC system, **b** experimental platform of the DIC system, **c** speckle pattern after spraying, **d** full-field strain distribution

$$MAER = \frac{1}{N}\sum_{m=1}^{N}\left(\frac{1}{3}\sum_{n=1}^{3}\left|\epsilon_{n,m}\right|\right) \tag{1}$$

$$SDER = \sqrt{\frac{1}{N}\sum_{m=1}^{N}\left(\frac{1}{3}\sum_{n=1}^{3}\left|\epsilon_{n,m}\right| - MAER\right)^{2}} \tag{2}$$

where ϵ, n, m, and N represent the strain, three strain components, measurement point, and number of measurement points, respectively. The MAER and SDER were 75.983 micro-strain and 67.719 micro-strain, respectively, which was lower than 150 micro-strain [45]. Because the algorithm causes a relatively large strain error at the edge of the region of interest (ROI), this study used a cropped edge approach to further reduce the error. Thus, the SDER should be lower than 67.179 micro-strain. This demonstrates that the DIC system used in this study has high measurement accuracy and precision.

3 Results and discussion

3.1 Tensile property

The engineering stress–strain curves in the uniaxial tensile tests are shown in Fig. 4. The documentation revealed a narrow scattering in the repeated uniaxial tensile tests. The ultimate tensile strength (UTS), 0.2% yield strength (YS),

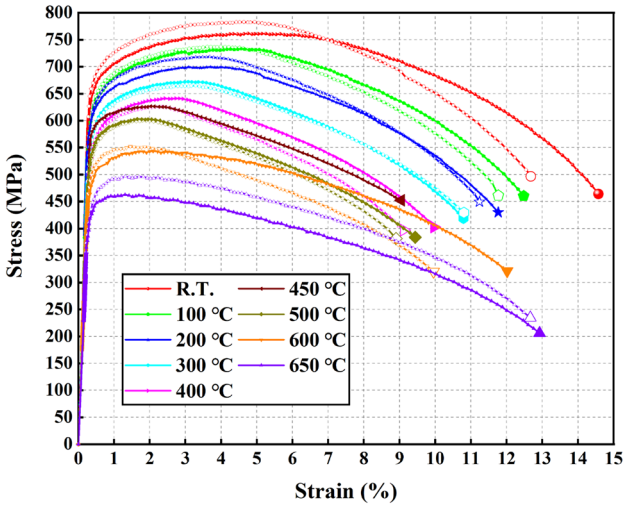

Fig. 4 (Color online) Engineering stress–strain curves in uniaxial tensile tests of CLF-1 steel measured at different tensile test temperatures

uniform elongation (UE), and total elongation (TE) of the studied steel at 25–650 ℃ are shown in Fig. 5. As the test temperature increased, the UTS, YS, and UE decreased, whereas the trend of the TE was different. The TE curve reached its lowest level when the temperature was approximately 450 ℃. This trend was consistent with other previous findings [46–48]. Notably, the YS and UTS changed with increasing temperature and had plateaus, whereas the TE changed with increasing temperature to a minimum value. This phenomenon was attributed to dynamic strain aging (DSA) [49–51]. DSA, which can be attributed to the interaction between mobile dislocations and diffusing solute atoms [50, 52], depends on the temperature and strain rate during uniaxial tensile tests, which control the diffusion of solute atoms and mobile dislocations, respectively. At 200–450 ℃, the reduction in the YS and UTS with increasing test temperature was retarded, namely the above-mentioned plateaus, which could be attributed to DSA-induced hardening. The reason for the existence of the minimum TE was DSA-induced embrittlement.

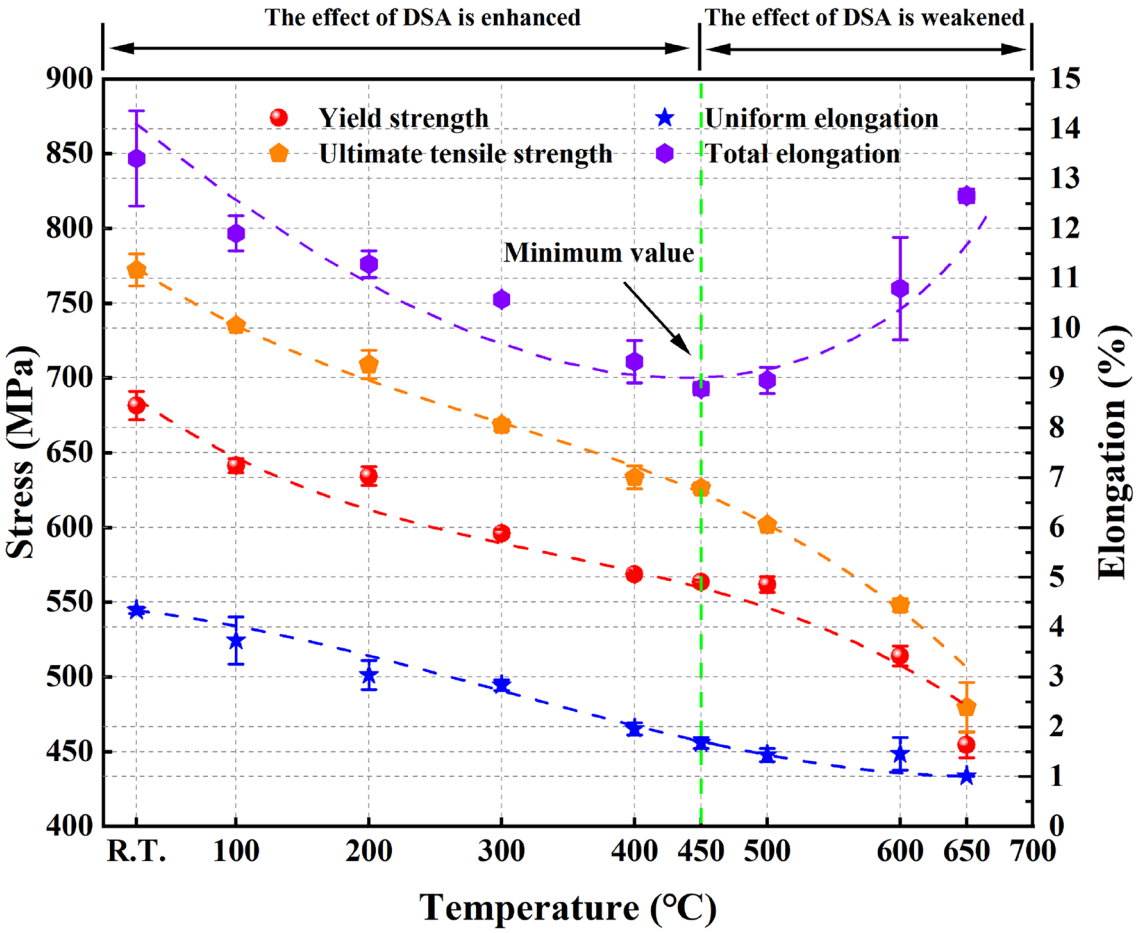

Fig. 5 (Color online) YS, UTS, UE, and TE of the studied steel at different test temperatures

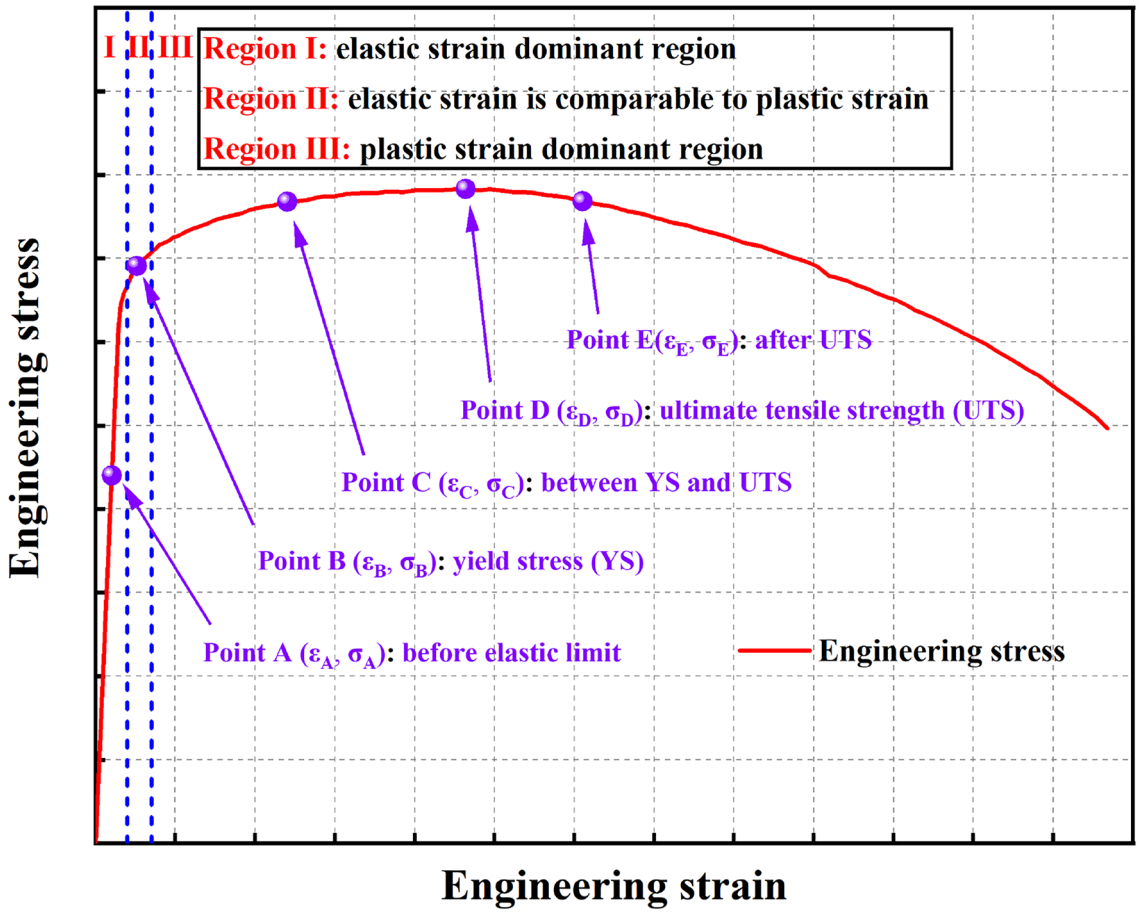

Fig. 6 (Color online) Different regions of the engineering stress–strain curve. Region I: elastic strain dominant region, region II: elastic strain comparable to the plastic strain region, region III: plastic strain dominant region

3.2 Strain distribution evolution during deformation

A schematic of the engineering stress–strain curve is shown in Fig. 6. The curve was divided into three regions: the elastic-dominant region (region I), elastic–plastic transition region (region II), and plastic-dominant region (region III). The statistics of the normalized strain (e_{yy}) distribution at points A, B, C, D, and E are shown in Fig. 7. Points A, B, C, D, and E were before the elastic limit, near the YS, between the YS and UTS, and after the UTS, respectively. The normalized methods were the strain at each point divided by the maximum strain, and the count at each strain interval divided by the total count. The mean strain (e_{yy}) values and variances at the different strain points are shown in Figs. 6 and 7 at different test temperatures which are presented in Fig. 8. The mean strain (e_{yy}) gradually increased as the tensile tests progressed, as shown in Fig. 8a, which was consistent with common sense. The variance also increased gradually as the tensile tests progressed, particularly after reaching the UTS, as depicted in Fig. 8b, which indicated that the strain localization was enhanced as the tensile test progressed. Additionally, the strain localization was also reflected in the strain distribution statistics, which are elaborated on in the next section.

It is widely known that the total strain (ϵ^{total}) consists of elastic strain ($\epsilon^{\text{elastic}}$) and plastic strain ($\epsilon^{\text{plastic}}$), $\epsilon^{\text{total}} = \epsilon^{\text{elastic}} + \epsilon^{\text{plastic}}$. In this study, the total strain (ϵ^{total}) was incorporated into the elastic strain ($\epsilon^{\text{elastic}}$) and plastic strain ($\epsilon^{\text{plastic}}$). We observed that the strain distribution followed a normal distribution in region I, when the strain distribution followed a lognormal distribution in region III. However, the strain distribution conformed to both the normal and lognormal distributions in region II. The normal distribution and lognormal distribution are represented by Eqs. (3) and (4), respectively.

$$y = y_0 + \frac{2A}{\sqrt{2\pi}w} e^{-\frac{2(x-x_c)^2}{w^2}} \tag{3}$$

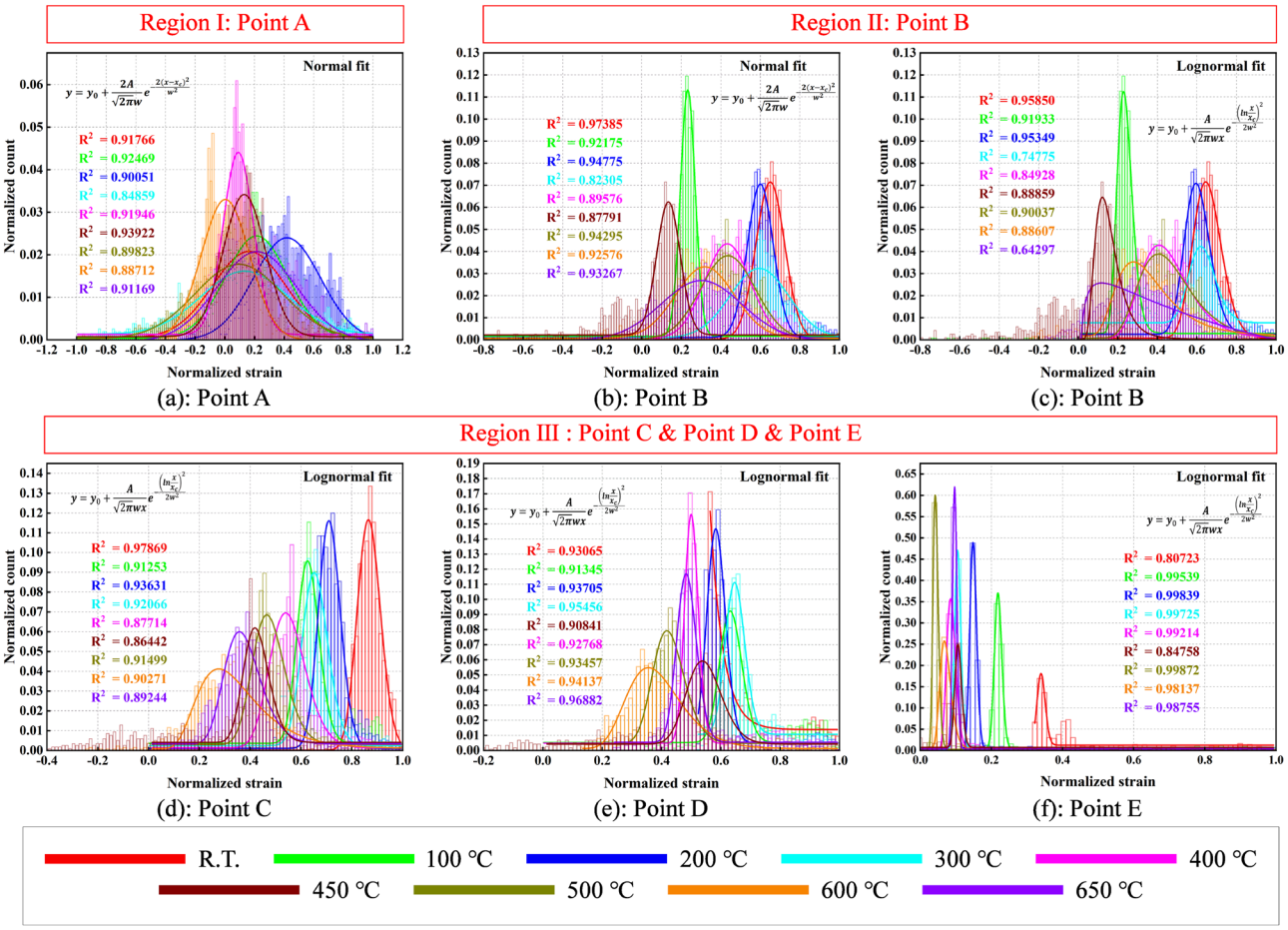

Fig. 7 (Color online) Normalized strain (e_{yy}) distribution at different test temperatures at (**a**) Point A (before the elastic limit), **b** Point B (near the YS), **c** Point B (near the YS), **d** Point C (between the YS and UTS), **e** Point D (at the UTS), and **f** Point E (after the UTS), respectively

$$y = y_0 + \frac{A}{\sqrt{2\pi}wx} e^{-\frac{\left(\ln\frac{x}{x_c}\right)^2}{2w^2}} \quad (4)$$

where y represents the probability density, w represents the standard deviation, x_c represents the mean value, x represents the median of each strain interval, and y_0 and A represent the fitting parameters. Most of the coefficients of determination were greater than 0.850, as shown in Fig. 7a–f, representing a good fit. Additionally, this meant that the strain distribution region studied in this study was larger than the MSRW of the studied steel and had statistical significance.

These findings held true for all the test temperatures in this study. To the best of our knowledge, this is the first study to report the statistics of the strain distribution during deformation at different temperatures. At point A, as shown in Fig. 6, the deformation could be considered purely elastic. Thus, the elastic strain obeyed a normal distribution [53] as shown in Fig. 7. At point B, which was in the elastic–plastic transition region, the numerical value of the plastic strain was comparable to the numerical value of the elastic strain. The strain distribution could be fitted using both normal and lognormal distributions owing to the strong interaction between the elastic strain and the occurrence of plastic strain, as depicted in Fig. 7b,c. Here, the strain accumulation process changed from following additive to following multiplicative. At point C, the numerical value of the elastic strain could not be compared with the numerical value of the plastic strain, that is, the plastic strain dominated; therefore, the strain distribution obeyed a lognormal distribution, as depicted in Fig. 7d. This was also why previous studies [30, 54] reported that the total strain conforms to a lognormal distribution during deformation. Additionally, the long "tail" in Fig. 7d–f corresponds to strong strain localization, which could be used to predict damage initiation [55, 56]. At points D and E, the strain distribution obeyed a lognormal distribution because the plastic strain dominated, as depicted in Fig. 7e, f.

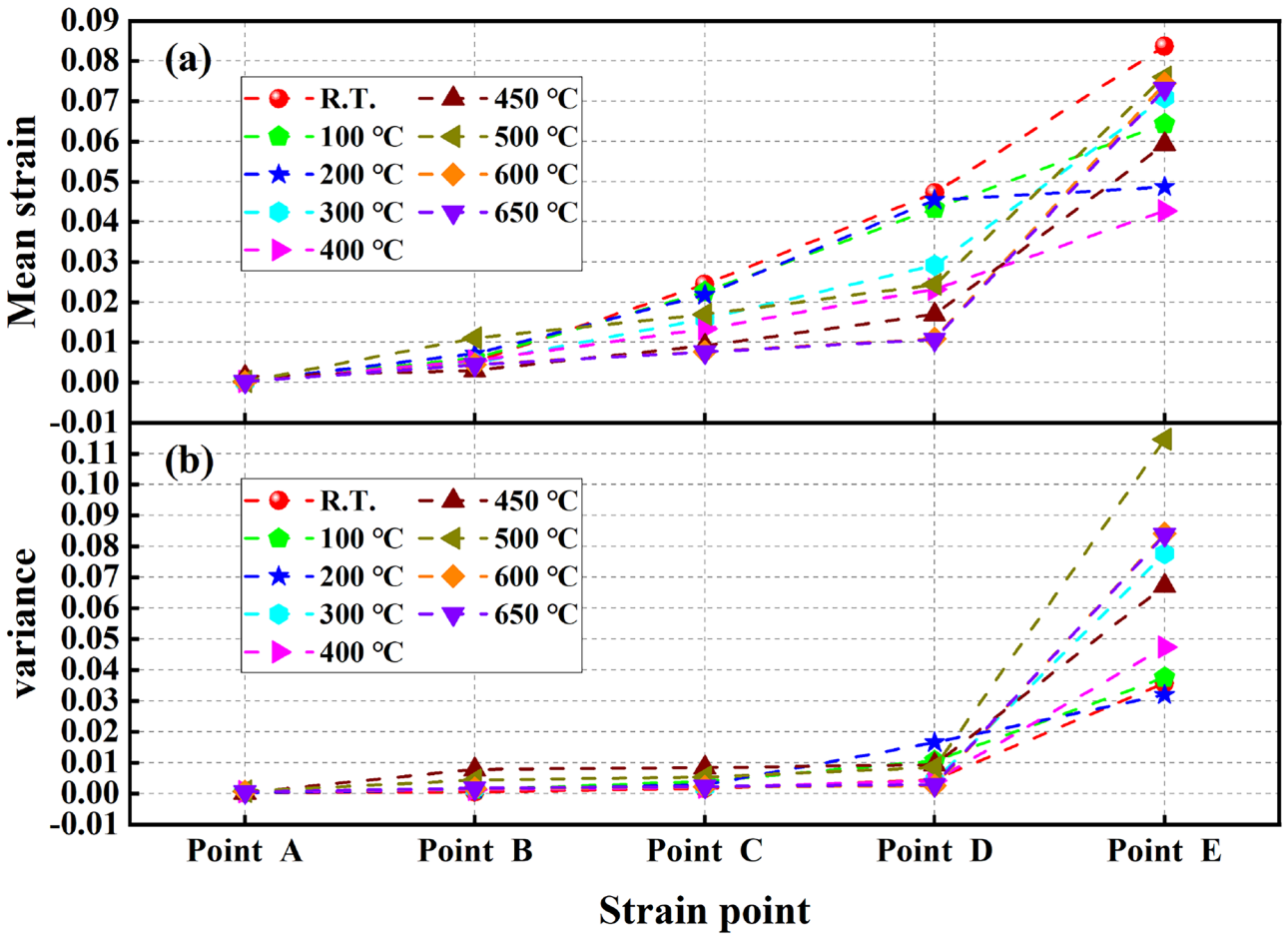

Fig. 8 (Color online) **a** Mean strain (e_{yy}) value and **b** strain (e_{yy}) variance at points A, B, C, D, and E at different test temperatures

Strain (e_{yy}) maps at points A, B, C, D, and E are shown in Fig. 9. Strain (e_{yy}) maps were cropped to eliminate the edge effect produced during the calculation. Typically, an uneven strain distribution occurs primarily during plastic deformation. However, a significantly uneven strain distribution appeared in the elastic stage (Point A), as shown in Fig. 9. This phenomenon can be attributed to the difference in the soft- and hard-phase deformations of the studied steel, as reported by Li et al. [57]. Significant strain concentration was observed, and strain-concentrated regions were approximately oriented at ±45° along the tensile direction at point B and point C, as shown in Fig. 9. This may be because shear stress had the maximum value at ±45° along the tensile direction. It was consistent with the results reported by Lindfeldt et al. [58], Gong et.al. [59], Wu et al. [60], and Tanaka et al. [54]. However, the strain-concentrated regions were not strict at ±45° along the tensile direction. The reason for this phenomenon may be the effects of the microstructure, such as the grain boundaries [61–65] and grain orientation [66, 67], which require further exploration. The alternating distributions of the high- and low-strain-concentrated regions in Fig. 9 were caused by the coordinated deformation of the microstructure during the initial stage of plastic deformation. Meanwhile, the strain in each region increased steadily, and the strain-concentrated regions did not expand significantly during uniform plastic deformation compared with those during elastic deformation. This can be attributed to strain-concentrated regions driving the entire uniform plastic deformation of the other regions. Necking occurred in the local strain-concentrated regions during non-uniform plastic deformation at points D and E. The strain was concentrated in the necking region, and the strain in the remaining parts gradually reduced until deformation stopped.

The strain (e_{yy}) distributions at points A, B, C, D, and E at different test temperatures are shown in Fig. 10. The strain (e_{yy}) distribution shifted to the right, the peak value of the strain value of the strain distribution gradually decreased, and the distribution gradually widened with the progress of the tensile tests at all test temperatures, as shown in Fig. 8a, b. The strain variances in the seven deformation states at 25–650 °C are shown in Fig. 11. To the best of our knowledge, the variance and strain localization were positively

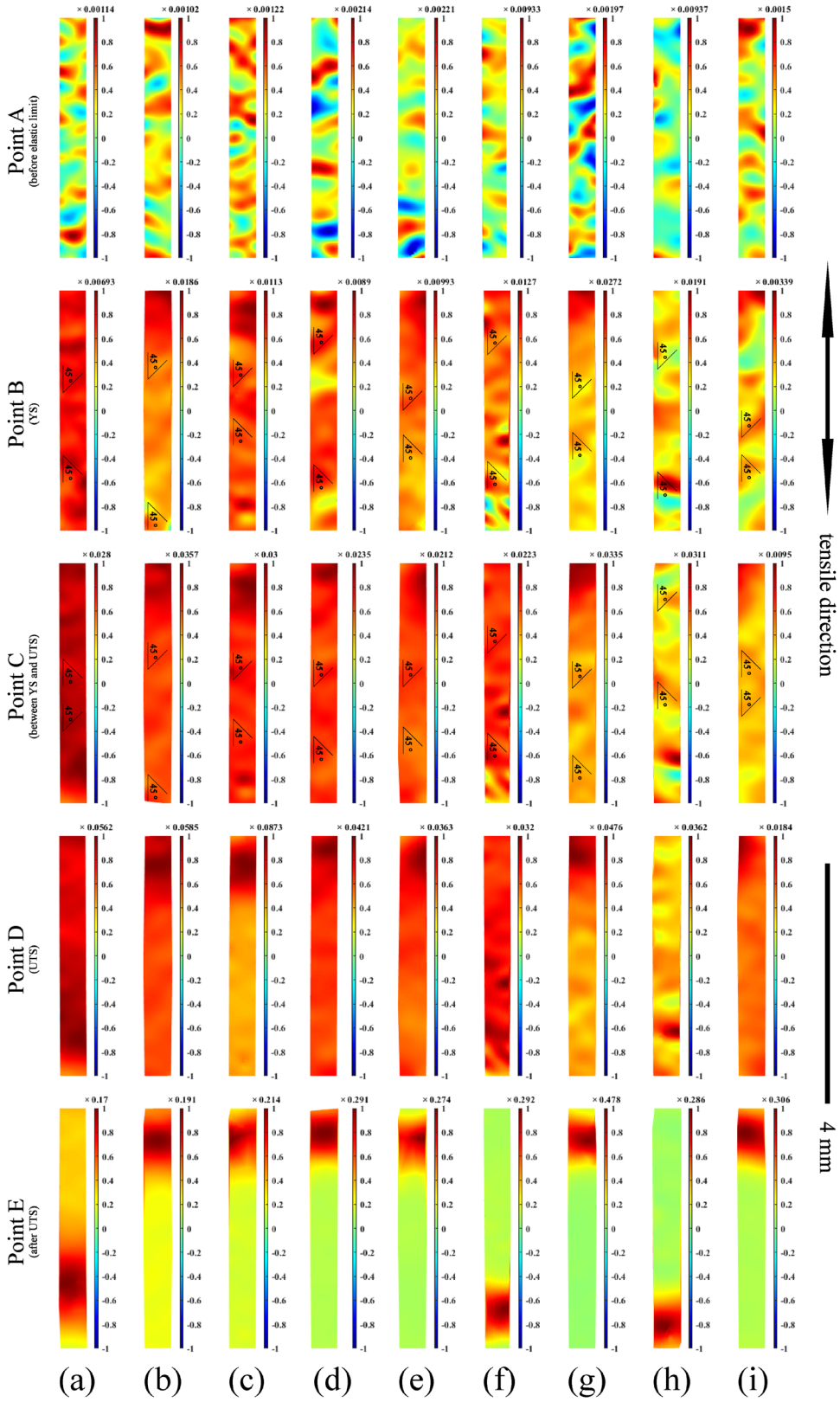

Fig. 9 (Color online) Equivalent strain (e_{yy}) maps from the uniaxial tensile tests using the DIC image of the ROI at different temperatures and stresses. **a** R.T., **b** 100 ℃, **c** 200 ℃, **d** 300 ℃, **e** 400 ℃, **f** 450 ℃, **g** 500 ℃, **h** 600 ℃, and **i** 650 ℃.

correlated; that is, the greater the variance, the stronger the strain localization. The strain variance first increased and then decreased with increasing test temperature, reaching a maximum value of approximately 450 °C in all deformation states, as shown in Fig. 11. Interestingly, the analysis in Sect. 3.1. A has shown that the decline rate of the YS

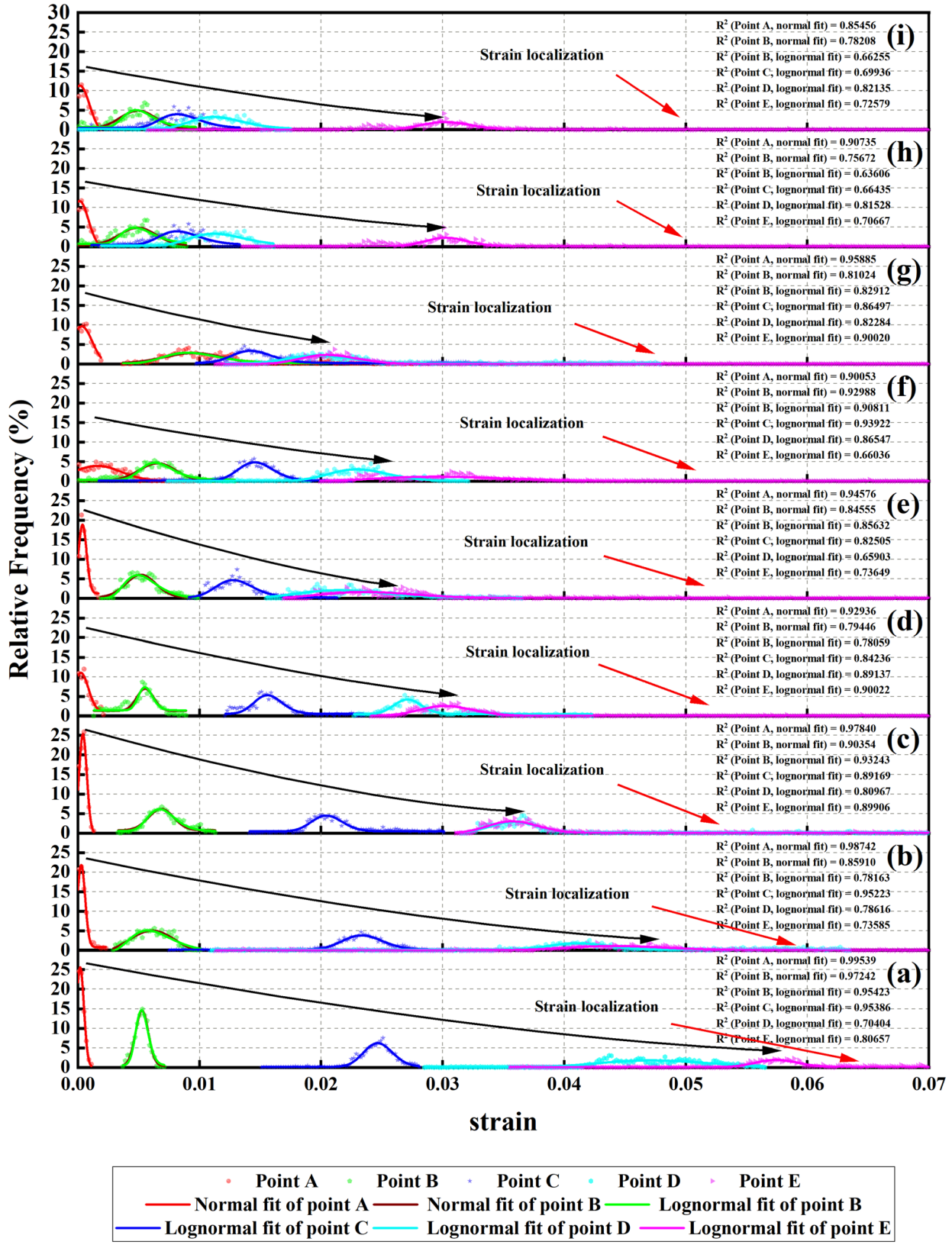

Fig. 10 (Color online) Normalized strain (e_{yy}) distribution at different deformations and temperatures. **a** R.T., **b** 100 ℃, **c** 200 ℃, **d** 300 ℃, **e** 400 ℃, **f** 450 ℃, **g** 500 ℃, **h** 600 ℃, **i** 650 ℃.

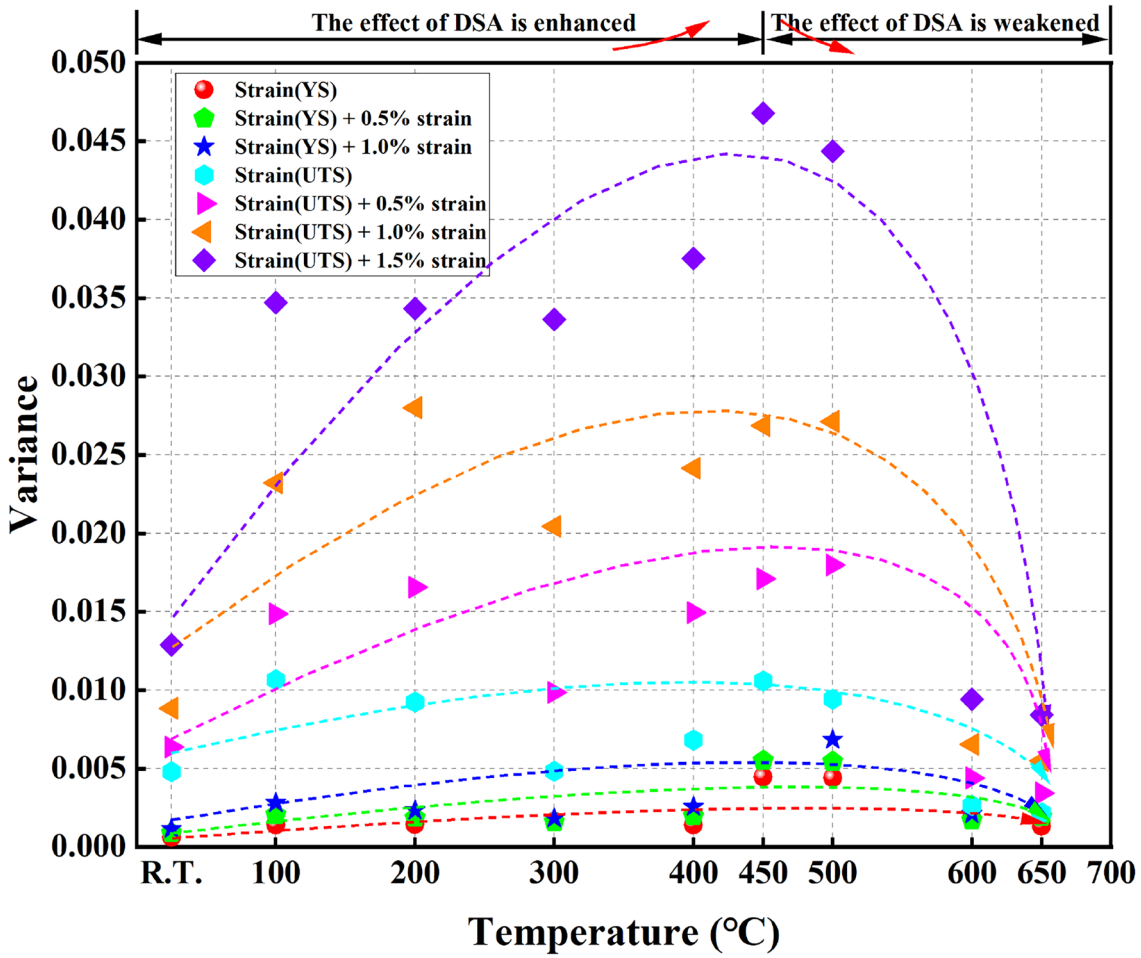

Fig. 11 (Color online) Relationship between variance of the fitted curves and test temperature

and UTS increased, and the TE reached the lowest value at approximately 450 °C with increasing test temperature owing to the effect of DSA as depicted in Fig. 5. With increasing test temperature, the variance increased; that is, the strain localization was enhanced, whereas the temperature was lower than 450 °C, possibly because the effect of DSA was enhanced with increasing test temperature. The interaction between the solute atoms and dislocations was enhanced. In contrast, with increasing test temperature, the variance decreased when the temperature was higher than 450 °C, possibly because the effect of DSA weakened with increasing temperature. The interaction between the solute atoms and dislocations was weakened. We believe that this discovery has general applicability to polycrystalline materials.

4 Conclusion

The effect of temperature on the strain distribution in the RAFM steel CLF-1 during deformation was explored using a uniaxial tensile test combined with DIC. The results provide a significant reference for mechanical engineering designs. The conclusions are as follows:

Strain localization region is alternately distributed in the direction of ± 45° along the tensile direction during plastic deformation because shear stress has a maximum value in the same direction and the coordinated deformation of microstructure within the temperature range from R.T. to 650 ℃.

A universal law of strain distribution exists because of the competition between plastic strain and elastic strain at all temperatures. The total strain obeys a normal distribution because the elastic strain dominates in region I. The total strain obeys both normal and lognormal distributions because the numerical value of the plastic strain is comparable to the numerical value of the elastic strain in region II.

The total strain obeys a lognormal distribution because the plastic strain dominates in the region III.

Strain localization has a strong relationship with temperature at the same engineering strain because of the effect of temperature on DSA. The stronger the effect of DSA, the stronger the strain localization. With increasing temperature, the stronger the strain localization at the same strain, the weaker the plasticity, that is, DSA-induced embrittlement, and the slower the strength decline, that is, DSA-induced hardening.

Acknowledgements The authors acknowledge the Experimental Center of Engineering and Material Sciences at the University of Science and Technology of China (USTC) for characterizing the specimens.

Author contributions All authors contributed to the study conception and design. Material preparation, data collection and analysis were performed by Shang-Ming Chen, Cheng-Jun Zhu, Yi-Fan Shi, and Lei Peng. The first draft of the manuscript was written by Shang-Ming Chen, Cheng-Jun Zhu, and Lei Peng, and all authors commented on previous versions of the manuscript. All authors read and approved the final manuscript.

Data Availability The data that support the findings of this study are openly available in Science Data Bank at https://cstr.cn/31253.11.sciencedb.j00186.00594 and https://doi.org/10.57760/sciencedb.j00186.00594.

Declarations

Conflict of interest The authors declare that they have no Conflict of interest.

References

1. J. Ongena, Nuclear fusion and its large potential for the future world energy supply. Nukleonika **61**, 425–432 (2016). https://doi.org/10.1515/nuka-2016-0070
2. S. Banacloche, A.R. Gamarra, Y. Lechon et al., Socioeconomic and environmental impacts of bringing the sun to earth: A sustainability analysis of a fusion power plant deployment. Energy **209**, 118460 (2020). https://doi.org/10.1016/j.energy.2020.118460
3. C. Huang, L. Li, Magnetic confinement fusion: a brief review. Front. Energy. **12**, 305–313 (2018). https://doi.org/10.1007/s11708-018-0539-1
4. N. Hashimoto, K. Kurosaki, Recent activities in the field of nuclear materials and nuclear fuels. J. Nucl. Sci. Technol. **56**, 147–149 (2019). https://doi.org/10.1080/00223131.2018.1544940
5. B. Raj, T. Jayakumar, Development of reduced activation ferritic-martensitic steels and fabrication technologies for indian test blanket module. J. Nucl. Mater. **417**, 72–76 (2011). https://doi.org/10.1016/j.jnucmat.2011.02.032
6. G. Qiu, D. Zhan, C. Li et al., Development of nano-structure china low-activation martensitic steel for fusion reactors. Mater. Lett. **252**, 248–251 (2019). https://doi.org/10.1016/j.matlet.2019.06.005
7. Q. Huang, X. Wang, S. Sun et al., Development of reduced activation ferritic/martensitic steels in China. J. Nucl. Mater. **568**, 153887 (2022). https://doi.org/10.1016/j.jnucmat.2022.153887
8. K. Shiba, M. Enoeda, S. Jitsukawa, Reduced activation martensitic steels as a structural material for ITER test blanket. J. Nucl. Mater. **329**, 243–247 (2004). https://doi.org/10.1016/j.jnucmat.2004.04.018
9. N. Baluc, R. Schäublin, P. Spätig et al., On the potentiality of using ferritic/martensitic steels as structural materials for fusion reactors. Nucl. Fusion **44**, 56 (2003). https://doi.org/10.1088/0029-5515/44/1/006
10. J. Yu, Q. Huang, F. Wan, Research and development on the china low activation martensitic steel (CLAM). J. Nucl. Mater. **367**, 97–101 (2007). https://doi.org/10.1016/j.jnucmat.2007.03.236
11. H. Tanigawa, E. Gaganidze, T. Hirose et al., Development of benchmark reduced activation ferritic/martensitic steels for fusion energy applications. Nucl. Fusion **57**, 092004 (2017). https://doi.org/10.1088/1741-4326/57/9/092004
12. L. Cai, X. Zeng, M. Liu et al., Preliminary development of a conceptual first wall for demo. Nucl. Fusion **60**, 096015 (2020). https://doi.org/10.1088/1741-4326/ab9f82
13. M. Kamaya, Y. Kawamura, T. Kitamura, Three-dimensional local stress analysis on grain boundaries in polycrystalline material. Int. J. Solids Struct. **44**, 3267–3277 (2007). https://doi.org/10.1016/j.ijsolstr.2006.09.020
14. X. Chen, W. Jiang, S. Lu et al., Nanoindentation behaviour simulation of a polycrystalline NiTi shape memory alloy using the crystal plastic finite element method. Mater. Today. Commun. **37**, 107292 (2023). https://doi.org/10.1016/j.mtcomm.2023.107292
15. F. Roters, P. Eisenlohr, L. Hantcherli et al., Overview of constitutive laws, kinematics, homogenization and multiscale methods in crystal plasticity finite-element modeling: Theory, experiments, applications. Acta Mater. **58**, 1152–1211 (2010). https://doi.org/10.1016/j.actamat.2009.10.058
16. Q. Fang, W. Lu, Y. Chen et al., Hierarchical multiscale crystal plasticity framework for plasticity and strain hardening of multi-principal element alloys. J. Mech. Phys. Solids **169**, 105067 (2022). https://doi.org/10.1016/j.jmps.2022.105067
17. F. Roters, M. Diehl, P. Shanthraj et al., Damask-the düsseldorf advanced material simulation kit for modeling multi-physics crystal plasticity, thermal, and damage phenomena from the single crystal up to the component scale. Comp. Mater. Sci. **158**, 420–478 (2019). https://doi.org/10.1016/j.commatsci.2018.04.030
18. F. Sun, E.D. Meade, N.P. O'Dowd, Microscale modelling of the deformation of a martensitic steel using the voronoi tessellation method. J. Mech. Phys. Solids **113**, 35–55 (2018). https://doi.org/10.1016/j.jmps.2018.01.009
19. J. Bai, Y. Huo, T. He et al., Modelling of mechanical response and microstructure evolution of EA4T steel during hot compression using the improved crystal plasticity finite element method. J. Mater. Eng. Perform. **33**, 2940–2951 (2024). https://doi.org/10.1007/s11665-023-08176-x
20. O. Casals, J. Očenášek, J. Alcala, Crystal plasticity finite element simulations of pyramidal indentation in copper single crystals. Acta Mater. **55**, 55–68 (2007). https://doi.org/10.1016/j.actamat.2006.07.018
21. H. Abdolvand, M.R. Daymond, C. Mareau, Incorporation of twinning into a crystal plasticity finite element model: Evolution of lattice strains and texture in zircaloy-2. Int. J. Plasticity. **27**, 1721–1738 (2011). https://doi.org/10.1016/j.ijplas.2011.04.005
22. D. Zhao, C. Xin, T. Jin et al., Evolution of face-centered-cubic polycrystalline plastic anisotropy under biaxial loading by crystal plasticity finite element method. Eng. Computation. **37**, 895–908 (2020). https://doi.org/10.1108/EC-12-2018-0573
23. L.Y. Si, L. Cheng, K. Tieu et al., Simulation of polycrystalline aluminum tensile test with crystal plasticity finite element method.

T. Nonferr. Metal. Soc. **17**, 1412–1416 (2007). https://doi.org/10.1016/S1003-6326(07)60286-6
24. C.C. Tasan, J.P. Hoefnagels, M. Diehl et al., Strain localization and damage in dual phase steels investigated by coupled in-situ deformation experiments and crystal plasticity simulations. Int. J. Plasticity. **63**, 198–210 (2014). https://doi.org/10.1016/j.ijplas.2014.06.004
25. Y. Liu, F. Van Der Meer, L.J. Sluys, A dispersive homogenization model for composites and its RVE existence. Comput. Mech. **65**, 79–98 (2020). https://doi.org/10.1007/s00466-019-01753-9
26. X. Shen, L. Gong, RVE model with porosity for 2D woven CVI SiC f/SiC composites. J. Mater. Eng. Perform. **25**, 5138–5144 (2016). https://doi.org/10.1007/s11665-016-2393-9
27. W. Zhang, J. Chen, H. Chen et al., Determination of RVE with consideration of the spatial effect. Int. J. Rock. Mech. Min. **61**, 154–160 (2013). https://doi.org/10.1016/j.ijrmms.2013.02.013
28. B. Koohbor, S. Ravindran, A. Kidane, Experimental determination of representative volume element (RVE) size in woven composites. Opt. Laser. Eng. **90**, 59–71 (2017). https://doi.org/10.1016/j.optlaseng.2016.10.001
29. S. Mirkhalaf, F.A. Pires, R. Simoes, Determination of the size of the representative volume element (RVE) for the simulation of heterogeneous polymers at finite strains. Finite Elem. Anal. Des. **119**, 30–44 (2016). https://doi.org/10.1016/j.finel.2016.05.004
30. A. Tang, H. Liu, G. Liu et al., Lognormal distribution of local strain: a universal law of plastic deformation in material. Phys. Rev. Lett. **124**, 155501 (2020). https://doi.org/10.1103/PhysRevLett.124.155501
31. H. Zhi, Z. Ma, L. Chen et al., Hydrogen-promoted heterogeneous plastic strain and associated hardening effect in polycrystalline nickel under uniaxial tension. Mat. Sci. Eng. A **894**, 146190 (2024). https://doi.org/10.1016/j.msea.2024.146190
32. W. Chen, W. He, B. Jiang et al., Revealing the effect of misorientation on the deformation behavior of a Mg-Y alloy from the perspective of local strain. Int. J. Plasticity. **170**, 103753 (2023). https://doi.org/10.1016/j.ijplas.2023.103753
33. P.P. Dhekne, T. Vermeij, V. Devulapalli et al., Micro-mechanical deformation behavior of heat-treated laser powder bed fusion processed Ti-6Al-4V. Scripta Mater. **233**, 115505 (2023). https://doi.org/10.1016/j.scriptamat.2023.115505
34. B. Peng, M. Zhang, D. Ye, Dic/dsi based studies on the local mechanical behaviors of HR3C/T92 dissimilar welded joint during plastic deformation. Mat. Sci. Eng. A **857**, 144073 (2022). https://doi.org/10.1016/j.msea.2022.144073
35. Y. Dai, X. Jia, R. Thermer et al., The second SINQ target irradiation program. STIP-II. J. Nucl. Mater. **343**, 33–44 (2005). https://doi.org/10.1016/j.jnucmat.2005.01.027
36. Y. Dai, R. Brun, W. Gao et al., The fourth SINQ target irradiation program. STIP-IV. J. Nucl. Mater. **431**, 2–9 (2012). https://doi.org/10.1016/j.jnucmat.2011.11.004
37. B. Li, Y. Dai, Tensile properties and microstructure of EC316LN irradiated in STIP-II. J. Nucl. Mater. **450**, 42–47 (2014). https://doi.org/10.1016/j.jnucmat.2014.02.009
38. Y. Dai, G. Bauer, Status of the first SINQ irradiation experiment. STIP-I. J. Nucl. Mater. **296**, 43–53 (2001). https://doi.org/10.1016/S0022-3115(01)00544-X
39. S.A. Maloy, T. Romero, M. James et al., Tensile testing of EP-823 and HT-9 after irradiation in STIP II. J. Nucl. Mater. **356**, 56–61 (2006). https://doi.org/10.1016/j.jnucmat.2006.05.003
40. S.W. Khoo, S. Karuppanan, C.S. Tan, A review of surface deformation and strain measurement using two-dimensional digital image correlation. Metrol. Meas. Syst. **23**, 461–480 (2016). https://doi.org/10.1515/mms-2016-0028
41. T. Nozawa, H. Sakasegawa, X. Chen et al., Non-contact strain evaluation for miniature tensile specimens of neutron-irradiated F82H by digital image correlation. Fusion Eng. Des. **157**, 111663 (2020). https://doi.org/10.1016/j.fusengdes.2020.111663
42. Y.L. Dong, B. Pan, A review of speckle pattern fabrication and assessment for digital image correlation. Exp. Mech. **57**, 1161–1181 (2017). https://doi.org/10.1007/s11340-017-0283-1
43. L. Liu, E.F. Morgan, Accuracy and precision of digital volume correlation in quantifying displacements and strains in trabecular bone. J. Biomech. **40**, 3516–3520 (2007). https://doi.org/10.1016/j.jbiomech.2007.04.019
44. G. Tozzi, E. Dall'Ara, M. Palanca et al., Strain uncertainties from two digital volume correlation approaches in prophylactically augmented vertebrae: Local analysis on bone and cement-bone microstructures. J. Mech. Behav. Biomed. **67**, 117–126 (2017). https://doi.org/10.1016/j.jmbbm.2016.12.006
45. W. Zhang, Damage behavior and fracture mechanism of lithium hydride ceramics under quasi-static loading at elevated temperatures. Ph.D. thesis, University of Science and Technology of China (2024). https://doi.org/10.27517/d.cnki.gzkju.2023.000538
46. H. Ge, L. Peng, Y. Dai et al., Tensile properties of CLAM steel irradiated up to 20.1 dpa in STIP-V. J. Nucl. Mater. **468**, 240–245 (2016). https://doi.org/10.1016/j.jnucmat.2015.10.040
47. J. Henry, X. Averty, Y. Dai et al., Tensile properties of 9Cr-1Mo martensitic steel irradiated with high energy protons and neutrons. J. Nucl. Mater. **318**, 215–227 (2003). https://doi.org/10.1016/S0022-3115(03)00119-3
48. E. Lucon, W. Vandermeulen, Overview of the tensile properties of EUROFER in the unirradiated and irradiated conditions. J. Nucl. Mater. **386**, 254–256 (2009). https://doi.org/10.1016/j.jnucmat.2008.12.109
49. H. Li, A. Nishimura, T. Nagasaka et al., Stress-strain behavior on tensile and low cycle fatigue tests of JLF-1 steel at elevated temperature in vacuum. Fusion Eng. Des. **81**, 2907–2912 (2006). https://doi.org/10.1016/j.fusengdes.2006.07.055
50. S.G. Hong, S.B. Lee, Dynamic strain aging under tensile and LCF loading conditions, and their comparison in cold worked 316L stainless steel. J. Nucl. Mater. **328**, 232–242 (2004). https://doi.org/10.1016/j.jnucmat.2004.04.331
51. P. Wang, J. Chen, H. Fu et al., Effect of N on the precipitation behaviours of the reduced activation ferritic/martensitic steel CLF-1 after thermal ageing. J. Nucl. Mater. **442**, S9–S12 (2013). https://doi.org/10.1016/j.jnucmat.2013.03.081
52. K. He, Y. Wang, H. Wang, Influence of dynamic strain aging on ferritic/martensitic steel and stability analysis. Fusion Eng. Des. **171**, 112581 (2021). https://doi.org/10.1016/j.fusengdes.2021.112581
53. J. Chen, A.M. Korsunsky, Why is local stress statistics normal, and strain lognormal? Mater. Des. **198**, 109319 (2021). https://doi.org/10.1016/j.matdes.2020.109319
54. M. Tanaka, Y. Yoshimi, K. Higashida et al., A multiscale approach for the deformation mechanism in pearlite microstructure: Experimental measurements of strain distribution using a novel technique of precision markers. Mat. Sci. Eng. A **590**, 37–43 (2014). https://doi.org/10.1016/j.msea.2013.09.072
55. X. Shang, H. Zhang, L. Wang et al., The effect of stress state and strain partition mode on the damage behavior of a mg-ca alloy. Int. J. Plasticity. **144**, 103040 (2021). https://doi.org/10.1016/j.ijplas.2021.103040
56. M. Li, W. Luo, Y. Chen et al., Full-field strain distribution and failure characteristics of CFRP-repaired steel structures. Eng. Fail. Anal. **115**, 104664 (2020). https://doi.org/10.1016/j.engfailanal.2020.104664
57. J. Li, Study on mechanical behaviors and microstructure evolution of medium manganese steel with high product of strength and plasticity during uniaxial tensile progress. Master's thesis,

Southwest Jiaotong University (2020). https://doi.org/10.27414/d.cnki.gxnju.2019.002790
58. E. Lindfeldt, M. Ekh, K. Cvetskovski et al., Using DIC to identify microscale strain fields from in-situ SEM images of a pearlitic steel. Exp. Mech. **54**, 1503–1513 (2014). https://doi.org/10.1007/s11340-014-9937-4
59. X. Gong, Z. Feng, D. Fan et al., Strain localization in titanium investigated via in situ digital image correlation with multiscale speckles. Mater. Charact. **189**, 111940 (2022). https://doi.org/10.1016/j.matchar.2022.111940
60. S. Wu, B. Bie, D. Fan et al., Dynamic shear localization of a titanium alloy under high-rate tension characterized by x-ray digital image correlation. Mater. Charact. **137**, 58–66 (2018). https://doi.org/10.1016/j.matchar.2018.01.011
61. X. Zhang, Y. Wang, J. Yang et al., Deformation analysis of ferrite/pearlite banded structure under uniaxial tension using digital image correlation. Opt. Laser. Eng. **85**, 24–28 (2016). https://doi.org/10.1016/j.optlaseng.2016.04.019
62. W. Gao, J. Lu, J. Zhou et al., Effect of grain size on deformation and fracture of inconel718: An in-situ SEM-EBSD-DIC investigation. Mat. Sci. Eng. A **861**, 144361 (2022). https://doi.org/10.1016/j.msea.2022.144361
63. J. Goulmy, D. Depriester, F. Guittonneau et al., Mechanical behavior of polycrystals: Coupled in situ DIC-EBSD analysis of pure copper under tensile test. Mater. Charact. **194**, 112322 (2022). https://doi.org/10.1016/j.matchar.2022.112322
64. B. Barkia, V. Doquet, E. Héripré et al., Characterization and analysis of deformation heterogeneities in commercial purity titanium. Mater. Charact. **108**, 94–101 (2015). https://doi.org/10.1016/j.matchar.2015.09.001
65. Y.J. Jin, H. Lu, C. Yu et al., Study on grain boundary character and strain distribution of intergranular cracking in the cghaz of t23 steel. Mater. Charact. **84**, 216–224 (2013). https://doi.org/10.1016/j.matchar.2013.08.004
66. K.I. Kim, Y. Oh, D.U. Kim et al., Strain analysis of multi-phase steel using in-situ EBSD tensile testing and digital image correlation. Met. Mater. Int. **28**, 1094–1104 (2022). https://doi.org/10.1007/s12540-021-01044-0
67. M.Y. Tseng, Y.C. Chao, Y.F. Hu et al., Semi in-situ investigations on deformation-induced micro-damage in high-strength dual-phase steels. Mater. Charact. **207**, 113547 (2024). https://doi.org/10.1016/j.matchar.2023.113547